Available online at www.sciencedirect.com
SCIENCE DIRECT®
International Journal of Heat and Mass Transfer 47 (2004) 5323–5338
International Journal of HEAT and MASS TRANSFER
www.elsevier.com/locate/ijhmt

A three-fluid model of two-phase dispersed-annular flow

V.M. Alipchenkov [a], R.I. Nigmatulin [b], S.L. Soloviev [c], O.G. Stonik [a], L.I. Zaichik [a,*], Y.A. Zeigarnik [a]

[a] *Institute for High Temperatures of the Russian Academy of Sciences, Krasnokazarmennaya 17a, 111250 Moscow, Russia*
[b] *Institute of Mechanics of the Ufa-Bashkortostan Branch of the Russian Academy of Sciences, Karl Marx Street 6, 450000 Ufa, Russia*
[c] *Centre of Software Development for NPPs and Reactor Facilities, MINATOM, P.O. Box 788, 101000 Moscow, Russia*

Received 16 March 2004; received in revised form 26 April 2004

Abstract

A three-fluid model of the dispersed-annular regime of two-phase flow is suggested. The model is based on the conservation equations of mass, momentum, and energy for the gas phase, the dispersed phase (droplets), and the film. Additionally, this model includes the equation for the number density of particles of the dispersed phase, which is used to determine the mean particle size. Calculations are compared with experimental data on the entrainment coefficient, film and droplet flow rates, film thickness, pressure drop, and droplet size.

Keywords: Three-fluid model; Annular flow; Droplet deposition; Liquid entrainment; Film; Coagulation; Breakup; Turbulence

1. Introduction

The available thermohydraulic computer codes (RELAP, TRAC, CATHARE, ATHLET etc.) are based on the so-called two-fluid models that include the conservation equations of mass, momentum, and energy for the liquid and gas phases. However, real two-phase and, the more so, multiphase media may consist of three and more components, for example, gas, droplets, and film in the dispersed-annular regime of flow. Therefore, it appears advisable to turn to a three-fluid model, with each component provided with its own set of conservation equations (e.g., see [1–4]).

In the formulation of the three-fluid model, each of the three phases is considered separately. The transition from a two-fluid to a three-fluid model of two-phase medium calls for the knowledge of mass flow rates between the droplets and the film, i.e., for the determination of the rates of the deposition of droplets onto the film and their entrainment (separation) from the film. This challenge implies a more thorough investigation of transport processes in two-phase media compared with the determination of the integral coefficient of entrainment (the ratio of the mass flow rate of droplets to the total flow rate of the liquid phase) appearing in two-fluid models. At present, the droplet deposition from turbulent flow in channels may be calculated within a fairly rigorous theoretical formulation that involves minimum empirical information about the structure of the near-wall turbulence (at least, in the absence of rebound of droplets and splashing of film). However, the process of liquid entrainment may be simulated only on

* Corresponding author. Fax: +7 095 362 55 90.
E-mail address: leonid.zaichik@mtu-net.ru (L.I. Zaichik).

0017-9310/$ - see front matter © 2004 Elsevier Ltd. All rights reserved.
doi:10.1016/j.ijheatmasstransfer.2004.07.011

Nomenclature

C_d	droplet drag coefficient
C_μ	Kolmogorov–Prandtl constant
C_{vm}	virtual mass coefficient
D	hydralic diameter of the channel
D_i	equivalent diameter of the gas-dispersed core
d	droplet diameter
E	entrainment coefficient
f_u	particle response coefficient
G	gravity parameter
g	gravity acceleration
k	kinetic turbulent energy of the gaseous phase
Lp	Laplace number
$\dot{m}$	superficial mass flow rate
$\dot{m}_L$	superficial mass flow rate of the liquid phase
N	droplet number density
P	pressure
R_D	deposition mass rate
R_E	entrainment mass rate
Re	Reynolds number
S	cross-section area of the channel
S_i	cross-section area of the gas-dispersed core
St	Stokes number
T_E	Eulerian integral time scale of turbulence
T_L	Lagrangian integral time scale of turbulence
T_{Lp}	time of interaction between particles and energy-containing eddies
t	time
U	velocity
U_G	superficial gas velocity
u_{1*}	friction velocity
$\langle u'^2 \rangle$	intensity of gas velocity fluctuations
$\langle v'^2 \rangle$	intensity of droplet velocity fluctuations
W	mass flow rate
We	Weber number
z	coordinate along the channel axis in the direction of the gas motion

Greek symbols

α	volume fraction
β_t	collision rate
Γ_{ij}	intensity of mass transfer from the ith to the jth phase
γ	drift parameter
δ	mean film thickness
ε	dissipation rate of turbulent energy
η	dynamic viscosity
ν	kinematic viscosity
ξ	friction factor
Π	perimeter of the internal surface of the channel
Π_i	interface perimeter of the gas-dispersed core
ρ	density
σ	surface tension
τ_{br}	total breakup time
τ_c	characteristic time between collisions of droplets
τ_{int}	interfacial friction stress on the film surface
τ_{ij}	friction stress on the interface between the ith and jth phases
τ_u	droplet response time
Φ	droplet volume fraction
φ	angle between the velocity and gravity vectors
χ	reflection coefficient (dimensionless)

Subscripts

br	breakup
int	interface
w	wall
l(2, 3)	gas (droplets, film)

the basis of a semi-empirical approach using some results of the theory of stability for a moving film.

Of key importance in the models of two-phase media is the description of the particle size of the dispersed phase (droplets, bubbles, slugs) or of the interfacial area. In the known thermohydraulic computer codes, the size of the dispersed phase is determined from empirical relations reflecting the effect of one or, at best, two mechanisms of the formation of the particle spectrum (for example, entrainment of droplets from a liquid film, fragmentation and coalescence of droplets or bubbles). For a more accurate description, it appears advisable to complement the calculation scheme with the transport equation for the particle number density of the dispersed phase, the introduction of which makes it possible to determine the size and the interfacial area of droplets or bubbles with due regard for different mechanisms of their formation, growth, and breakup. The employment of the transport equation for the particle number density has, in our opinion, certain advantages over the application of the corresponding equation of the interfacial area [5,6]. In particular, unlike the interfacial area, the particle number density does not alter during phase transitions, and the equation for the number density has a simpler form than that for the interfacial area.

This paper deals with a three-fluid model of two-phase annular flow, which is based on the one-dimensional balance equations of mass, momentum, and

energy for each of three "fluids", namely, the gas phase, the dispersed phase (droplets), and the film. The model includes the transport equation for the variation of the number density of droplets due to deposition, entrainment, coagulation, and breakup. The results of predictions are compared with experimental data for isothermal annular flows in tubes.

2. Balance equations for mass and momentum

The three-fluid model of annular flow is based on one-dimensional balance equations for mass, momentum, and energy, written separately for each of three "fluids", namely, the gas (vapor), the dispersed phase (droplets), and the film. The balance equations of mass for a channel of uniform cross-section have the form

$$\frac{\partial \alpha_1 \rho_1}{\partial t} + \frac{\partial \alpha_1 \rho_1 U_1}{\partial z} = -\Gamma_{12} + \Gamma_{21} - \Gamma_{13} + \Gamma_{31}, \tag{1}$$

$$\frac{\partial \alpha_2 \rho_2}{\partial t} + \frac{\partial \alpha_2 \rho_2 U_2}{\partial z} = \Gamma_{12} - \Gamma_{21} - \Gamma_{23} + \Gamma_{32}, \tag{2}$$

$$\frac{\partial \alpha_3 \rho_3}{\partial t} + \frac{\partial \alpha_3 \rho_3 U_3}{\partial z} = \Gamma_{13} - \Gamma_{31} + \Gamma_{23} - \Gamma_{32}. \tag{3}$$

Here, Γ_{ij} stands for the rate of mass transfer from the ith to the jth phase. In particular, Γ_{12} and Γ_{21} designate mass transfer between the gas and dispersed phases due to condensation of vapor on droplets or evaporation of droplets, Γ_{13} and Γ_{31} denote mass transfer between the gas phase and the liquid film because of vapor condensation or liquid evaporation, and Γ_{23} and Γ_{32} identify the rate of mass transfer between the dispersed phase and the film as a result of deposition and entrainment of droplets, respectively,

$$\Gamma_{23} = \frac{\Pi_i}{S} R_D, \quad \Gamma_{32} = \frac{\Pi_i}{S} R_E,$$

where the interface perimeter Π_i is related to the perimeter of the internal surface of the channel Π as $\Pi_i = (1-\alpha_3)^{1/2}\Pi$.

The balance equations for momentum are written as follows:

$$\begin{aligned}&\frac{\partial \alpha_1 \rho_1 U_1}{\partial t} + \frac{\partial \alpha_1 \rho_1 U_1^2}{\partial z} \\ &= -\alpha_1 \frac{\partial P}{\partial z} - \Gamma_{12} U_{12} + \Gamma_{21} U_{21} - \Gamma_{13} U_{13} + \Gamma_{31} U_{31} \\ &\quad + \alpha_1 \rho_1 g \cos\varphi - \frac{6\alpha_2}{d}\tau_{12} - \frac{\Pi_i}{S}\tau_{13},\end{aligned} \tag{4}$$

$$\begin{aligned}&\frac{\partial \alpha_2 \rho_2 U_2}{\partial t} + \frac{\partial \alpha_2 \rho_2 U_2^2}{\partial z} \\ &= -\alpha_2 \frac{\partial P}{\partial z} + \Gamma_{12} U_{12} - \Gamma_{21} U_{21} + \Gamma_{23} U_{23} + \Gamma_{32} U_{32} \\ &\quad + \alpha_2 \rho_2 g \cos\varphi + \frac{6\alpha_2}{d}\tau_{12} - \frac{\Pi_i}{S}\tau_{23},\end{aligned} \tag{5}$$

$$\begin{aligned}&\frac{\partial \alpha_3 \rho_3 U_3}{\partial t} + \frac{\partial \alpha_3 \rho_3 U_3^2}{\partial z} \\ &= -\alpha_3 \frac{\partial P}{\partial z} + \Gamma_{13} U_{13} - \Gamma_{31} U_{31} + \Gamma_{23} U_{23} - \Gamma_{32} U_{32} \\ &\quad + \alpha_3 \rho_3 g \cos\varphi + \frac{\Pi_i}{S}(\tau_{13} + \tau_{23}) - \frac{\Pi}{S}\tau_{3w}.\end{aligned} \tag{6}$$

In Eqs. (4)–(6) U_{ij} is the velocity which has the matter of the ith phase during its transition to the jth phase, τ_{ij} designates the friction stress on the interface between the ith and jth phases, and τ_{3w} stands for the friction stress between the film and the wall.

In accordance with asymptotic solutions under conditions of strong blowing and suction [7], it is assumed that, in the case of evaporation, the vapor leaves the liquid with a velocity corresponding to that of the liquid phase, while during condensation the vapor decelerates in a narrow boundary layer to the velocity of the liquid phase. Therefore, the condensing vapor leaves the gaseous phase also with a velocity characteristic of the liquid phase. The streamwise velocity of the droplets depositing on the film surface is taken to be equal to their velocity in the flow core, that is, the deceleration of deposing droplets in the neighborhood of the film is ignored, because it does not appear possible to consistently include this effect in the one-dimensional formulation. The streamwise velocity, with which the droplets separate from the film surface and are entrained by the gas flow, is assumed to be equal to the mean film velocity. Therefore, the values of velocities on the interfaces in the balance equations for momentum (4)–(6) are taken as

$$U_{21} = U_{12} = U_{23} = U_2, \quad U_{31} = U_{13} = U_{32} = U_3.$$

The processes of heat transfer and phase transitions are not treated in this paper, therefore, no balance equations for energy are given. To close the set of equations (1)–(6) we should determine the interfacial and wall friction, as well as the mass flow rates of droplet deposition and entrainment.

3. Interfacial and wall friction

The interfacial friction on the gas–droplets interface is defined by the relation

$$\tau_{12} = \frac{\rho_2 (U_1 - U_2) d}{6\tau_u},$$

in which the dynamic response time of a droplet is given by

$$\tau_u = \frac{4(\rho_2 + C_{vm}\rho_1)d}{3\rho_1 C_d |U_1 - U_2|},$$

$$C_d = \begin{cases} \frac{24}{Re_d}(1 + 0.15 Re_d^{0.687}) & \text{for } Re_d \leqslant 10^3, \\ 0.44 & \text{for } Re_d > 10^3. \end{cases}$$

Here, C_d is the droplet drag coefficient, C_{vm} is the virtual mass coefficient taken as 0.5, and $Re_d \equiv |U_1 - U_2| d/\nu_1$ is the Reynolds number for the droplet.

The separate determination of the friction stress on the film interface for the gas phase, τ_{13}, and for the droplets, τ_{23}, is a fairly difficult problem from the experimental standpoint. Therefore, these quantities may be determined only with a relatively high error, which is probably responsible for the large difference between the values given by different empirical dependences for the interfacial friction coefficient.

The friction stress on the gas-film interface is defined as

$$\tau_{13} = \frac{\xi_{13}\alpha_1\rho_1(U_1 - U_3)^2}{8(1-\alpha_3)}. \tag{7}$$

Many correlations are available in the literature to evaluate the friction factor ξ_{13} [2,8–13]. All these correlations are based, to some or other extent, on the analogy with sand roughness, within which it is assumed that the height of the waves that are formed on the film surface is related to the mean film thickness δ. The best-known and most verified correlation is the one of Wallis [8], which directly accounts for the effect of "wave roughness" in terms of the film thickness δ related to the hydraulic diameter of the channel D:

$$\xi_{13} = 0.02(1 + 300\bar{\delta}), \quad \bar{\delta} = \delta/D. \tag{8}$$

Later on, in a number of studies, correlation (8) was modified to provide the limiting transition of it to single-phase flows

$$\xi_{13} = \xi_{10}(1 + 300\bar{\delta}), \tag{9}$$

where ξ_{10} is the friction factor in a channel with solid smooth walls that is a function on the Reynolds number of the gas flow $Re_1 \equiv \rho_1 U_1 D_i/\eta_1$.

However, Eq. (9) does not describe the flows with fully developed effects of roughness, when the friction factor must not depend on the Reynolds number. In order to describe the interfacial friction in the entire range of variation of $\bar{\delta}$ (that is, from the single-phase flow with $\bar{\delta} = 0$ to the flow with relatively thick films), we can use the following correlation which combines (8) and (9):

$$\xi_{13} = \xi_{10} + 6\bar{\delta}, \quad \xi_{10} = (1.82\lg Re_1 - 1.64)^{-2}. \tag{10}$$

Note that the correlation for ξ_{13} given by Nigmatulin [2] appears to be close to (10). The relations proposed by Henstock and Hanratty [9] and Fukano and Furukawa [12] predict too high values of ξ_{13} for relatively thick films. As was indicated by Fore et al. [13] and Fossa et al. [14], the simple correlation of Wallis corresponds to experimental data better than the more complicated relations of Henstock and Hanratty [9], Asali et al. [10], and Ambrosini et al. [11]. Therefore, further we will use Eq. (10) for the calculation of the interfacial friction factor.

To evaluate the friction stress of droplets with the film, we can invoke the correlation between the intensities of turbulent fluctuations of the velocities of the dispersed and carrier phases in the approximation of homogeneous turbulence [15]

$$\langle v'^2\rangle = f_u\langle u'^2\rangle, \quad f_u = \frac{1 + A\tau_u/T_{\mathrm{Lp}}}{1 + \tau_u/T_{\mathrm{Lp}}},$$
$$A = \frac{(1 + C_{\mathrm{vm}})\rho_1/\rho_2}{1 + C_{\mathrm{vm}}\rho_1/\rho_2}, \tag{11}$$

where $\langle v'^2\rangle$ and $\langle u'^2\rangle$ are the intensities of velocity fluctuations of the dispersed and carrier phases, f_u is the coefficient of response of the particles to the turbulent velocity fluctuations of the carrier phase, and T_{Lp} is the time of interaction between the particles and the energy-containing eddies.

Eq. (11) is used to derive the following formula for the droplets-film friction stress:

$$\tau_{23} = \frac{\alpha_2\rho_2(U_2 - U_3)^2}{\alpha_1\rho_1(U_1 - U_3)^2} f_u\tau_{13}. \tag{12}$$

The eddy-droplet interaction time is determined by the following approximations [16]:

$$T_{\mathrm{Lp}} = T_{\mathrm{Lp}}(St = 0) + [T_{\mathrm{Lp}}(St = \infty) - T_{\mathrm{Lp}}(St = 0)]F(St), \tag{13}$$

$$T_{\mathrm{Lp}}(St = 0) = T_{\mathrm{L}}\frac{4(3\alpha + 3\alpha^2/2 + 1/2)}{5\alpha(1+\alpha)^2},$$
$$\alpha = \sqrt{1 + \gamma^2 + \frac{2\gamma}{\sqrt{3}}},$$
$$T_{\mathrm{Lp}}(St = \infty) = T_{\mathrm{L}}\frac{6(2+\gamma)}{5(1+\gamma)^2},$$
$$F(St) = \frac{St}{1+St} - \frac{5St^2}{4(1+St)^2(2+St)}.$$

Here, $St \equiv \tau_u/T_{\mathrm{E}}$ is the Stokes number that quantifies the droplet inertia and thereby measures the degree of coupling between the gas and dispersed phases, T_{L} is Lagrangian integral time scale of turbulence, T_{E} is Eulerian time macroscale of turbulence in the moving coordinate system, $\gamma \equiv |U_1 - U_2|/u_{1*}$ is the drift parameter, and $u_{1^*} \equiv \sqrt{\tau_{13}/\rho_1}$ is the friction velocity. Eq. (13) takes into account the effect of the inertia of droplets as well as of the so-called crossing-trajectories effect due to the mean droplet velocity drift relative to the gas on the eddy-droplet interaction time. As it follows from (13), for inertialess particles ($St = \gamma = 0$), T_{Lp} coincides with the Lagrangian time scale T_{L}. In the absence of the mean drift ($\gamma = 0$), T_{Lp} monotonically increases with increasing St from the Lagrangian time scale T_{L} for $St = 0$ to the Eulerian macroscale for $St = \infty$. As the drift parameter γ increases, T_{Lp} decreases monotonically. The time scales of turbulence, which are averaged over the channel cross-section, are taken as $T_{\mathrm{L}} = 0.04D_i/u_{1*}$ and

$T_E = 0.1D_i/u_{1*}$, where $D_i \equiv (1-\alpha_3)^{1/2}D$ is the equivalent diameter of the gas-dispersed core.

The friction stress between the film and the wall is defined as

$$\tau_{3w} = \frac{\xi_{3w}\rho_3 U_3^2}{8},$$
$$\xi_{3w} = \begin{cases} \dfrac{1+G}{1+2G/3}\dfrac{64}{Re_3} & \text{for } Re_3 < 1600, \\ \xi_{30} = (1.82\lg Re_3 - 1.64)^{-2} & \text{for } Re_3 > 1600. \end{cases} \quad (14)$$

In (14), $Re_3 \equiv 4W_3/\Pi\eta_3$ is the Reynolds number for the liquid film, $W_3 \equiv \alpha_3\rho_3 U_3 S$ is the mass flow rate of the film, $G \equiv (\rho_3 - \rho_{12})g\cos\varphi\,\delta/\tau_{int}$ is the gravity parameter, $\rho_{12} = \alpha_1\rho_1 + \alpha_2\rho_2$ is the density of the gas–droplet flow, and $\tau_{int} = \tau_{12} + \tau_{13}$ is the interfacial friction stress on the film surface. The friction factor ξ_{3w} allows for the fact that, under conditions of laminar flow, the velocity profile in the liquid film is formed under the effect of both the interfacial friction and the gravity force. Under conditions of turbulent flow, the effect of external forces on ξ_{3w} is fairly week, that is, the film velocity profile can be considered as being universal, and consequently the friction factor in (14) is determined by the same approximation as in (10).

Note that this paper does not deal with the regimes with low gas flow rates when flooding or flow reversal may occur, because these phenomena call for special-purpose analysis. Therefore, the film flow regimes considered are restricted to the condition of $|G| < 1$.

In the absence of the liquid film, expressions (7) and (12) for the interfacial friction stresses are transformed into the corresponding relations for the wall friction when taking $\delta = U_3 = 0$.

4. Deposition of droplets

Experimental data show that in annular flows we almost always have fairly inertial (large) droplets, whose response time exceeds the eddy-droplet interaction time. In [17], an analytical model for predicting the rate of deposition of inertial particles from turbulent flow in a vertical tube is proposed. This model is based on a solution of governing equations along with appropriate boundary conditions, which stem from a kinetic equation for the probability density function of the droplet velocity distribution in turbulent flow. In our paper, this model is modified to calculate the deposition of droplets from the core of the two-phase annular turbulent flow in a vertical channel.

In the approximation of high-inertia particles, the asymptotic solution of the equation of motion of the dispersed phase gives the following expression for the mass deposition rate:

$$R_D = \frac{8\Phi\tau_u\langle v_r'^2\rangle}{D_i}\left[1 + \left(\frac{1-\chi}{1+\chi}\sqrt{\frac{2}{\pi}} + 4\sqrt{\frac{\pi}{2}}\frac{1+\chi}{1-\chi}\right)\frac{8\tau_u\langle v_r'^2\rangle^{1/2}}{D_i}\right]^{-1}, \quad (15)$$

where $\langle v_r'^2\rangle$ is the droplet fluctuating velocity intensity in the radial direction, χ is the coefficient of reflection (rebound) of droplets from the wall or from the film surface (in the case of complete adsorption $\chi = 0$, and in the case of complete reflection of droplets $\chi = 1$).

In [17], a set of algebraic equations is given for the axial, radial, and circumferential components of the fluctuating velocity of the dispersed phase. From this set of equations, it follows that, in the absence of interparticle collisions, any component of the droplet velocity fluctuations can be found independently; hence, to calculate the deposition rate, according to (15), it is sufficient to determine the radial intensity of the droplet velocity fluctuations $\langle v_r'^2\rangle$. However, in the case of significant contribution of interparticle collisions to the turbulent energy balance of the dispersed phase, in order to calculate the deposition rate we must, strictly speaking, solve the entire set of equations for the axial, radial, and circumferential fluctuating velocities. For simplicity, to avoid solving the entire set of equations for the individual components of the droplet velocity fluctuations, we will assume the correlation between the turbulent energy k_2 and the radial intensity of the velocity fluctuations $\langle v_r'^2\rangle$ in the form of $k_2 = 3\langle v_r'^2\rangle$ that is characteristic in the single-phase near-wall turbulence. Calculations performed testify that the assumption made has no significant effect on the accuracy of predicting the deposition rate. The interactions of the droplets during collisions with one another as well as with the wall are taken to be inelastic; therefore, the respective coefficients of momentum restitution are taken to be zero. In view of the assumptions made, the following equation is derived from [17] for the radial droplet fluctuating velocity:

$$\left(1 + \frac{\tau_u}{9\tau_{c1}}\right)\langle v_r'^2\rangle + 4\sqrt{\frac{2\langle v_r'^2\rangle^3}{\pi}}\frac{\tau_u}{D_i} = \frac{T_{Lp}}{T_L}\frac{C_r u_{1*} D_i}{2\tau_u}. \quad (16)$$

Here, the constant C_r is taken to be equal to 5/81, and the characteristic time between collisions of droplets in the core of the annular flow is determined by the relation

$$\tau_c = \left(\frac{2\pi}{\langle v_r'^2\rangle}\right)^{1/2}\frac{5d}{72\Phi}. \quad (17)$$

Eqs. (16) and (17) yield the following explicit formula for $\langle v_r'^2\rangle$, which interpolates the asymptotic dependences for $\tau_u \to 0$ and $\tau_u \to \infty$:

$$\langle v_r'^2\rangle = \left(\frac{T_{Lp}}{T_L}\frac{C_r u_{1*} D_i}{2\tau_u}\right)\left\{1 + \left[\frac{T_{Lp}}{T_L}\frac{16 C_r u_{1*} D_i \tau_u}{\pi}\left(\frac{\Phi}{5d_p} + \frac{1}{D_i}\right)^2\right]^{1/3}\right\}^{-1}. \quad (18)$$

As is seen from (18), the fluctuating velocity of droplets and, consequently, the rate of their deposition decrease with increasing the droplet fraction in the gas-dispersed core. This effect is caused by the dissipation of turbulent droplet velocity fluctuations due to inelastic collisions. However, as was demonstrated in [17], the main factor causing the decrease in the deposition rate with increasing droplet fraction is the rise of droplet size due to coalescence, which results in reducing the degree of droplet involvement in the turbulent motion of the carrier gas flow. Note that the decrease in the deposition coefficient with increasing the fraction of inertial droplets is supported by many of known experimental data [18–20]. It should be also mentioned that, according to (15) and (18), the deposition rate of large drops, whose response time is compared to the characteristic time of the energy-containing eddies, is decreases with increasing droplet inertia. This is attributed to reducing droplet involvement in fluctuating motion of a carrier turbulent flow as the droplet inertia increases and is also connected with the "crossing trajectories" effect due to gravity.

The interaction between depositing droplets and the surface bounding the gas-dispersed flow (solid wall or liquid film) is characterized by the reflection coefficient χ. In the case of droplet deposition on the walls of a dry vertical channel which is free of the liquid film, almost no rebound of droplets is observed, and, hence, the reflection coefficient may be taken to be zero. On the contrary, in the presence of a thick film on the channel wall, rebound and splashing (secondary entrainment) are observed, and, consequently, the reflection coefficient may become close to unity. The parameter governing the reflection coefficient of droplets during deposition is based on the Weber number $We_{\delta i} \equiv \tau_i \delta/\sigma$, which specifies the film resistance to failure. It is apparent that the limiting relations to be hold are the following:

$$\chi \to 0 \quad \text{for } We_{\delta i} \to 0, \qquad \chi \to 1 \quad \text{for } We_{\delta i} \to \infty. \tag{19}$$

Based on the results of comparison with experimental data, the reflection coefficient is given in the form

$$\chi = 1 - \exp(-3We_{\delta i}), \tag{20}$$

which satisfies relations (19).

5. Entrainment of droplets

Under conditions of annular flow of a gas–liquid system in channels, several mechanisms of droplet entrainment from the film occur [2]. The dynamic impact of the gas-dispersed core causes the generation of waves on the film surface, with droplets being separated and entrained from the crests of these waves. In the presence of droplets in the flow core, entrainment in the form of secondary droplets (splashes) is possible due to the impact of primary droplets deposing on the film. We will effectively account for the secondary entrainment by introducing the reflection coefficient of droplets during deposition calculations according to (20). Finally, in a heated channel with nucleate boiling in the film, entrainment can occur due to the action of vapor bubbles which induce splashing however in our paper we do not consider this mechanism of entrainment.

In order to calculate the dynamic entrainment of droplets under the impact of moving gas-dispersed flow, we have to determine the critical conditions of the onset of film atomization. In experiments, these conditions are found as a result of extrapolation to zero of the mass entrainment rate R_E, when the atomization of the film and the separation of droplets emerge. A number of empirical and semi-empirical correlations were suggested in the literature for predicting the critical parameters and the rate of dynamic droplet entrainment. Obviously, the most correct correlations must include primarily the properties of the liquid film and the interface. The Weber number $We_{\delta i}$ and the Reynolds number Re_3 for the film may be selected as suitable criteria for describing droplet entrainment.

Hewitt and Govan [21] proposed the following equation for the critical film Reynolds number:

$$Re_3^* = \exp\left[5.85 + 0.425\frac{\eta_1}{\eta_3}\sqrt{\frac{\rho_3}{\rho_1}}\right]. \tag{21}$$

Droplet entrainment originates when the agitating interfacial shear force exerted by the gas flowing over the film exceeds the force of surface tension that retains the film. Consequently, the critical Weber number can be considered as a criterion of inception of atomization. In [22], it is recommended to use for $We_{\delta i}$ the following relation:

$$\frac{We_{\delta i}^*}{(\eta_3/\eta_1)(\rho_1/\rho_3)^{1/2}} = \begin{cases} 1.9 \times 10^{-3} Re_3^{0.2} & \text{for } Re_3 < 1200, \\ 0.7 \times 10^{-5} Re_3 & \text{for } Re_3 > 1200. \end{cases} \tag{22}$$

In Fig. 1, the shaded regions indicate the variation in the critical Reynolds and Weber numbers, which are calculated, according to Eqs. (21) and (22), with a change in the physical properties (viscosity and density) of water and steam on the saturation line in the pressure range from 0.1 to 15 MPa.

Correlation (22) predicts a monotonic growth of $We_{\delta i}^*$ with an increase in Re_3. However, there is a number of experimental data (for example, see [19,23,24]), which point to the existence of the critical film Reynolds number below which almost no entrainment of droplets is observed. In [25], an energy analysis of the stability of the film flow to finite perturbations was performed. The results obtained demonstrate a relatively week effect of the angle of inclination of the channel with respect to

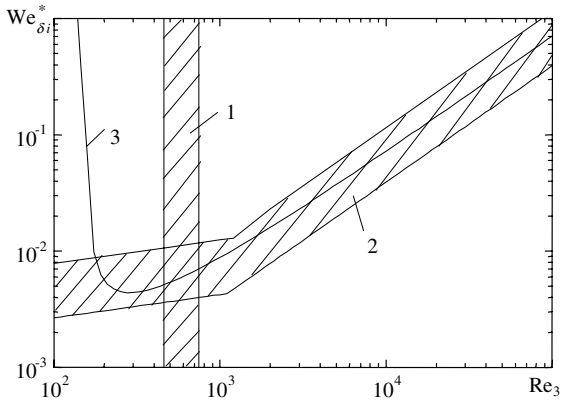

Fig. 1. The critical film Weber number as a function of the film Reynolds number. 1, 2, and 3: Predictions by (21)–(23).

the gravity vector as well as of the flow direction (upward or downward) on the critical Reynolds number and give a mean value of $Re_3^* = 160$.

Note that Ishii and Grolmes [26] recommended $Re_3^* = 160$ as the critical film Reynolds number of the onset of droplet entrainment for horizontal and upward flows, whereas Nigmatulin et al. [24] gave the value of $Re_3^* = 180$ for upward flow.

We can see from Fig. 1 that the part of the parameter $(\eta_3/\eta_1)(\rho_1/\rho_3)^{1/2}$, which allows for the effect of the ratio of the physical properties of the liquid and gas phases, may be quite significant, especially in relation (22). However, Eqs. (21) and (22) demonstrate the directly opposite effect of this parameter on the entrainment onset. Therefore, we will ignore the effect of this parameter and use the following simple dependence of the critical film Weber number on the Reynolds number:

$$We_{\delta i}^* = [7 \times 10^{-6} + 4 \times 10^{-4}(Re_3 - 160)^{-0.8}]Re_3. \qquad (23)$$

This correlation accounts for the theoretical value of $Re_3^* = 160$ and agrees well with formula (22) at high values of Re_3. According to (23), function $We_{\delta i}^*(Re_3)$ is nonmonotonic, it has a minimum and increases linearly at high values of Re_3 (see Fig. 1).

Two types of dependences for describing the droplet entrainment rate appear to be best validated theoretically, namely, those based on the deviation of the film Reynolds number Re_3 from its critical value Re_3^* or on the deviation of the film Weber number $We_{\delta i}$ from the respective critical value $We_{\delta i}^*$. The correlation of Hewitt and Govan [21]

$$\frac{R_E}{\alpha_1 \rho_1 U_1} = \begin{cases} 5.75 \times 10^{-5}\left[\left(\frac{\rho_3}{\rho_1}\right)^2 \frac{(Re_3 - Re_3^*)^2}{Lp_{D3}}\right]^{0.316} & \text{for } Re_3 > Re_3^*, \\ 0 & \text{for } Re_3 < Re_3^*, \end{cases} \qquad (24)$$

is a dependence of the first type. Here $Lp_{D3} \equiv \rho_3 \sigma D/\eta_3^2$ is the Laplace number, and Re_3^* is determined according to (21).

Lopez de Bertodano and Assad [27] suggested the following correlation based on the Kelvin–Helmholtz instability theory:

$$\frac{R_E D}{\eta_3} = \begin{cases} 4.47 \times 10^{-7}\left[We_{D1}\left(\frac{\rho_3 - \rho_1}{\rho_1}\right)^{1/2}(Re_3 - Re_3^*)\right]^{0.925}\left(\frac{\eta_1}{\eta_3}\right)^{0.26} & \text{for } Re_3 > Re_3^*, \\ 0 \quad \text{for } Re_3 < Re_3^*, \end{cases} \qquad (25)$$

where $We_{D1} \equiv \rho_1 U_1^2 D/\sigma$ is the Weber number constructed by the gas flow velocity. The critical Reynolds number Re_3^* in (25) is taken to be 80.

Nigmatulin et al. [22] assumed that the entrainment of droplets emerges at the instant when the interfacial shear stress exceeds the surface tension force. Therefore, the Weber number of the film is a suitable criterion to describe entrainment, and the deviation $We_{\delta i}$ from the critical value $We_{\delta i}^*$ is used as the parameter that governs the entrainment rate. In [22], the following correlation was proposed:

$$\frac{R_E \Pi (1-\alpha_3)^{1/2}}{\eta_3} = \begin{cases} 0.55\left(\frac{\rho_3}{\rho_1}\right)^{0.5} \frac{(We_{\delta i} - We_{\delta i}^*)^{0.85}}{\Omega_3^{0.7} Re_3} & \text{for } We_{\delta i} > We_{\delta i}^*, \\ 0 & \text{for } We_{\delta i} < We_{\delta i}^*, \end{cases} \qquad (26)$$

where $\Omega_3 \equiv \eta_3 (g/\rho_3 \sigma^3)^{1/4}$ and $We_{\delta i}^*$ is determined in accordance with (22).

Finally, a simple correlation of the same type as (26) was suggested in [25]

$$R_E = \begin{cases} 0.023(\rho_3 \tau_i)^{1/2}(We_{\delta i} - We_{\delta i}^*) & \text{for } We_{\delta i} > We_{\delta i}^*, \\ 0 & \text{for } We_{\delta i} < We_{\delta i}^*, \end{cases} \qquad (27)$$

where $We_{\delta i}^*$ is determined by (23). It is also based on the Kelvin–Helmholtz instability theory and fits the experimental data reported in [28].

6. Equation for the droplet number density

In annular flow, the spectrum of droplet sizes is usually very wide. Such a wide spectrum is formed as a result of different physical processes, namely, breakup, coalescence, phase changes, film atomization, and droplet deposition. It depends on the initial droplet size distribution at the inlet to a channel. For the sake of simplicity, we will simulate the droplet size spectrum in the frame of a monodisperse approximation. With this assumption, the equation for the droplet number

density, N, is invoked, and the droplet size distribution is taken into account by means of introducing certain fixed values of the ratios of the surface, volume, and Sauter mean diameters to the maximum diameter. These values are taken as $d_{20}/d_{\max} = 0.11$, $d_{30}/d_{\max} = 0.14$, $d_{32}/d_{\max} = 0.25$. They follow from the upper log-normal distribution with the mean parameters recommended by Azzopardi [29]. The volume mean droplet diameter is defined as $d_{30} = (6\Phi/\pi N)^{1/3}$.

The equation for the droplet number density is given in the form

$$\frac{\partial \rho_2 S_i N}{\partial t} + \frac{\partial \rho_2 S_i U_2 N}{\partial z} = K_{\mathrm{br}} - K_{\mathrm{coag}} + Q_{\mathrm{E}} - Q_{\mathrm{D}}, \tag{28}$$

where $S_i \equiv S(1-\alpha_3)$ is the cross-section area of the gas-dispersed core. The terms on the right-hand side of (28) allow for, respectively, the variation in the number of droplets due to breakup, coagulation, entrainment, and deposition. Breakup and coagulation are treated as the volume processes, whereas entrainment and deposition are considered as the surface ones.

The breakup of droplets is described by means of the relaxation model

$$K_{\mathrm{br}} = \rho_2 S_i \frac{N_{\mathrm{br}} - N}{\tau_{\mathrm{br}}} H(N_{\mathrm{br}} - N). \tag{29}$$

In (29), $H(x)$ is the Heaviside function: $H(x<0) = 0$ and $H(x>0) = 1$. The number density N_{br} corresponds to the number of droplets per unit volume with the volume mean diameter $d_{30,\mathrm{br}}$, which is determined with the assumption that the breakup is a result of the droplet interaction with the gas flow

$$N_{\mathrm{br}} = \frac{6\Phi}{\pi d_{30,\mathrm{br}}^3}. \tag{30}$$

The quantity τ_{br} in (29) characterizes the time of fragmentation of droplets. In accordance with (29), no breakup is observed when $N > N_{\mathrm{br}}$ ($d_{30} < d_{30,\mathrm{br}}$), while, at $d_{30} > d_{30,\mathrm{br}}$, N exponentially tends to the equilibrium value of the droplet number density N_{br}, with the characteristic time being τ_{br}. Fragmentation of droplets in a gas flow may be governed by two mechanisms. First, under the impact of the aerodynamic drag force, the mean velocity difference (slip) between the gaseous and dispersed phases causes deformation of a droplet, which may lead to its destruction. This mechanism of breakup is characterized by the Weber number $We^{\mathrm{a}}_{\mathrm{d12}} \equiv \rho_1 (U_1 - U_2)^2 d/\sigma$ constructed using the difference between the gas and droplet velocities and may be even observed under conditions of laminar flow in the absence of turbulent velocity fluctuations. The other mechanisms of breakup is associated with the interaction between the droplet and turbulent eddies and may take place in the absence of the mean velocity slip.

According to experimental dada reported in [2,30,31], the critical Weber number $We^{\mathrm{a}^*}_{\mathrm{d12}}$, which is the criterion of the droplet stability to any disturbances and the onset of its fragmentation under the impact of the aerodynamic drag force due to the mean velocity slip, can be given by the following correlation:

$$We^{\mathrm{a}^*}_{\mathrm{d12}} = 12\left(1 + 1.5 Lp_{\mathrm{d2}}^{-0.37}\right), \tag{31}$$

in which $Lp_{\mathrm{d2}} \equiv \rho_2 \sigma d/\eta_2^2$ is the Laplace number for the droplet.

The total breakup time of a particle is the sum of the time of deformation of the droplet interface up to a critical state and the time of its disintegration into fragments [32]

$$\tau_{\mathrm{br}} = \tau_{\mathrm{def}} + \tau_{\mathrm{dris}}. \tag{32}$$

In the case of droplet fragmentation due to the mean velocity slip, the deformation time can be estimated as [2,32]

$$\tau^{\mathrm{a}}_{\mathrm{def}} = \frac{d}{|U_1 - U_2|}\left(\frac{\rho_2}{\rho_1}\right)^{1/2}. \tag{33}$$

The disintegration time is assumed to be equal to the reciprocal of the lower natural frequency of droplet oscillations [33]

$$\tau_{\mathrm{dris}} = \frac{\pi d^{3/2}(3\rho_2 + 2\rho_1)^{1/2}}{4(3\sigma)^{1/2}}. \tag{34}$$

If the critical Weber number based on the mean velocity difference between the gas and droplets is known, we can determine the stable droplet diameter, above which the fragmentation will occur,

$$d^{\mathrm{a}}_{\mathrm{br}} = \frac{We^{\mathrm{a}^*}_{\mathrm{d12}}(d^{\mathrm{a}}_{\mathrm{br}})\sigma}{\rho_1 (U_1 - U_2)^2}. \tag{35}$$

However, using criterion (35) we obtain, as a rule, much larger droplet sizes compared with those observed experimentally in the annular two-phase flow. Therefore, the mechanism of breakup induced by the interaction of droplets with turbulent eddies of the carrier gas seems to be more probable. To describe the breakup of droplets by turbulence, the well-known hypothesis of Kolmogorov–Hinze is invoked. It is based on the assumption that breakup is essentially controlled by turbulent structures, whose sizes are close to the particle diameter (because only such velocity fluctuations are capable to cause large deformation of the droplet interface), and occurs when the disruptive turbulent stresses are larger than the confining stresses due to surface tension. With such a model, a permissible maximal stable particle size is determined from the following relations:

$$We^{\mathrm{t}}_{\mathrm{d}}(d^{\mathrm{t}}_{\mathrm{br}}) = We^{\mathrm{t}^*}_{\mathrm{d}}, \quad We^{\mathrm{t}}_{\mathrm{d}}(d) = \frac{\rho_1 S_{ll}(d) d}{\sigma}, \tag{36}$$

where $We^{\mathrm{t}}_{\mathrm{d}}$ is the droplet Weber number based on the longitudinal two-point velocity structure function S_{ll} [34]. Then, by definition, $S_{ll}(d)$ determines the difference

in velocities at two points separated by the length, which is equal to the droplet diameter d. The critical Weber number in (36) is as follows:

$$We_{\mathrm{d}}^{\mathrm{t}^*} = \frac{3}{f_{\mathrm{r}}(1+2\rho_2/\rho_1)}, \quad f_{\mathrm{r}} = \frac{1+A\tau_u/T_{\mathrm{Lr}}}{1+\tau_u/T_{\mathrm{Lr}}}. \tag{37}$$

Here, T_{Lr} is the time scale that specifies the fluctuating velocity increment at two points separated by d [35]. The expression for f_{r} in (37) coincides with f_u in (11) when replacing T_{Lr} by T_{Lp}. For low-inertial particles (droplets or bubbles) when $f_{\mathrm{r}} \simeq 1$, (37) reduces to the relation [36]

$$We_{\mathrm{d}}^{\mathrm{t}^*} = A = \frac{3}{1+2\rho_2/\rho_1}, \tag{38}$$

which correlates well with the critical Weber number predicted by the well-known resonance hypotheses for the splitting of droplets and bubbles by turbulence [37].

The velocity structure function in (36) and the two-point time scale in (37) are given by the corresponding approximations that interpolate those in the viscous, inertial, and external space subranges [38]:

$$S_{ll}(d) = \left[\left(\frac{15\nu_1}{\varepsilon_1 d^2}\right)^n + \left(\frac{1}{2(\varepsilon_1 d)^{2/3}}\right)^n + \left(\frac{3}{4k_1}\right)^n\right]^{-1/n},$$

$$T_{\mathrm{Lr}} = \left[\frac{1}{(5\nu_1/\varepsilon_1)^{n/2} + \left(0.3d^{2/3}/\varepsilon^{1/3}\right)^n} + \left(\frac{1}{T_{\mathrm{Lp}}}\right)^n\right]^{-1/n}, \quad n = 20. \tag{39}$$

In (39), k_1 and ε_1 are the kinetic turbulent energy and the energy dissipation rate of the carrier gas flow, respectively. They are determined as follows:

$$k_1 = \frac{u_{1^*}^2}{C_\mu^{1/2}}, \quad \varepsilon_1 = C_\mu^{1/2}\frac{k_1}{T_{\mathrm{L}}} = 25\frac{u_{1^*}^3}{D_i},$$

where $C_\mu \equiv 0.09$ is the Kolmogorov–Prandtl constant.

Then relations (36) along with (37) and (39) provide an equation to determine the maximal stable diameter of droplets due to their interaction with turbulent eddies

$$d_{\mathrm{br}}^{\mathrm{t}} = \frac{We_{\mathrm{d}}^{\mathrm{t}^*}(d_{\mathrm{br}}^{\mathrm{t}})\sigma}{\rho_1 S_{ll}(d_{\mathrm{br}}^{\mathrm{t}})}. \tag{40}$$

The characteristic time of droplet deformation due to interaction with turbulent eddies is estimated by means of the Newton law under the assumption that the deformation force is proportional to the difference between the turbulent and surface tension stresses. As a result, this time is given by

$$\tau_{\mathrm{def}}^{\mathrm{t}} = b\left[\frac{(1+2\rho_2/\rho_1)We_{\mathrm{d}}^{\mathrm{t}^*}}{(1-We_{\mathrm{d}}^{\mathrm{t}^*})/We_{\mathrm{d}}^{\mathrm{t}}}\right]^{1/2}\frac{d}{S_{ll}^{1/2}}, \quad b = 1.1. \tag{41}$$

Note that the deformation time (41) correlates with that found by Martinez-Bazán et al. [39] for the air bubbles injected into a turbulent water flow field. Therefore, the constant b is determined from the requirement to fit the experiments [39], with, according to (38), $We_{\mathrm{d}}^{\mathrm{t}^*} = 3$ for large bubbles at $\rho_2/\rho_1 \ll 1$.

Taking into account both mechanisms of fragmentation, the maximum stable size of droplets may be determined as the minimal value given by (35) and (40), that is, $d_{\mathrm{br}} = \min\left(d_{\mathrm{br}}^{\mathrm{a}}, d_{\mathrm{br}}^{\mathrm{t}}\right)$. The droplet breakup time is obtained from (32)–(34) and (41) in accordance with the minimal value of the droplet diameter thus obtained. Note that in all correlations associated with droplet breakup except for (30), namely in (31)–(41) we should use the maximum diameter $d_{\max}$.

In the monodisperse approximation, the averaged velocities of all droplets have the same values at any space point; therefore, the droplets may coagulate only as a result of collisions due to turbulent velocity fluctuations. Note that, in this case, the contribution of the Brownian diffusion and several other mechanisms, which are significant for coagulation of fine aerosol particles, is minor. In subsequent developments, droplets are supposed to stick together when once collided, and therefore the droplet collision rate is treated as the coagulation rate, that is, the coagulation efficiency coefficient is taken to be unity. Then, the term describing the coagulation in (28) has the form

$$K_{\mathrm{coag}} = -\frac{\rho_2 S_i \beta_{\mathrm{t}} N^2}{2} \tag{42}$$

To find the collision rate β_{t} in (42), we invoke the assumption that the joint probability density of the velocities of the gas and the droplet is a correlated Gaussian distribution. Then we can derive the following analytical expression for the collision rate induced by droplet–turbulence interaction [38,40]:

$$\beta_{\mathrm{t}} = 4\left(\frac{2\pi}{3}\right)^{1/2} d^2 k_1^{1/2}[f_u(1-f_u)]^{1/2}. \tag{43}$$

In view of expression (11) for the coefficient of response of droplets to turbulent velocity fluctuations of the carrier gas with $\rho_1/\rho_2 \ll 1$, Eq. (43) is rewritten as

$$\beta_{\mathrm{t}} = 4\left(\frac{2\pi}{3}\right)^{1/2}\frac{d^2 u_{1^*}}{C_\mu^{1/4}}\left(\frac{\tau_u}{T_{\mathrm{Lp}}}\right)^{1/2}\left(1+\frac{\tau_u}{T_{\mathrm{Lp}}}\right)^{-1}. \tag{44}$$

The droplet–eddy interaction time T_{Lp} in (44) is calculated in accordance with (13). As it follows from (44), β_{t} reaches its maximal value at $\tau_u = T_{\mathrm{Lp}}$. A decrease in β_{t} with increasing τ_u for large droplets is attributed to their reduced involvement in the turbulent motion of the carrier gas, which is the cause for collisions. A decrease in β_{t} with decreasing τ_u for small droplets is associated with an increase in the correlation of their motion leading

to a decrease in the collision frequency. Since the collision rate is proportional to the collision section of droplets, the surface mean diameter d_{20} is taken to be the characteristic droplet diameter for all quantities in (44).

An increase in the droplet number density due to liquid entrainment from the film is defined by the relation

$$Q_{\mathrm{E}} = \Pi_{\mathrm{i}} \frac{\rho_2}{\rho_3} \frac{R_{\mathrm{E}}}{\vartheta_{\mathrm{E}}} \cong \Pi_{\mathrm{i}} \frac{R_{\mathrm{E}}}{\vartheta_{\mathrm{E}}}.$$

To determine the mean volume of entrained droplets $\vartheta_{\mathrm{E}} \equiv \pi d_{30,E}^3/6$, we will use the simple assumption of instantaneous fragmentation of droplets penetrating into the flow core from the film under the impact of the aerodynamic drag force due to the difference between the gas and film velocities. Then, relations similar to (31) and (35) yield the following expression for the maximum diameter of droplets penetrating into the gas-dispersed core from the film:

$$d_{\max,\mathrm{E}} = \frac{We^*_{\mathrm{d}13}(d_{\max,\mathrm{E}})\sigma}{\rho_1 (U_1 - U_3)^2},$$

$$We^*_{\mathrm{d}13} = 12\left(1 + 1.5 Lp_{\mathrm{d}3}^{-0.37}\right), \quad Lp_{\mathrm{d}3} = \frac{\rho_3 \sigma d_{\max,\mathrm{E}}}{\eta_3^2}.$$

A decrease in the droplet number density due to deposition is represented as

$$Q_{\mathrm{D}} = \Pi_{\mathrm{i}} R_{\mathrm{D}} \frac{N}{\Phi},$$

where the Sauter droplet diameter d_{32} is used for calculating the mass deposition rate R_{D}.

7. Calculation results

In the dispersed-annular flow in channels, the liquid wall layer and the gas–droplet core stream move concurrently. The liquid layer, which has an agitated wavy surface, can be atomized and entrained by the gas, and simultaneously the droplets can deposit on the wall. Therefore, the net entrainment of droplets may be interpreted as a balance between the deposition and entrainment phenomena. It is clear that, in sufficiently long channels, an equilibrium sets in between the processes of deposition, entrainment, coagulation, and fragmentation of droplets, and as a result a hydrogynamically developed flow is realized, with none of the flow parameters varying along the channel length. The calculation results are analyzed for the inlet section of the channel as well as for the region of hydrogynamically stabilized flow.

The motion of a three-fluid (gas–droplets–film) system is calculated using the balance equations for mass (1)–(3) momentum (4)–(6) and droplet number density (28) with due regard for closure relations given above. Adiabatic downward and upward vertical annular flows are analized in a wide range of the determining parameters (pressure, mass flow rate, and void fraction). With a view to investigate the influence of the prediction accuracy of droplet entrainment on the flow characteristics, calculations were performed for all four alternatives of the correlation for the entrainment rate, as given by Eqs. (24)–(27). Moreover, calculations were also performed with the simple correlations for the deposition rate given by Hewitt and Govan [21] and Nigmatulin et al. [22] instead of Eq. (15) along with (18) and (20). This was done to analyze the effect of the prediction accuracy of droplet deposition on the flow characteristics. These correlations for the deposition rate, combined with any dependence for the entrainment rate of Eqs. (24)–(27) produce significantly poorer results as to agreement with experimental data, than those obtained by means of Eq. (15) along with (18) and (20). Therefore, all the calculation results presented below were obtained by means of Eq. (15) along with (18) and (20) for the deposition rate, and all four alternatives of the calculation procedures differ from one another only by the correlation for the entrainment rate, with the rest of the closure relations remaining the same.

Fig. 2 shows variation in the film flow rate under conditions of the upward air–water flow experimentally investigated by Nigmatulin et al. [24]. In the experiments, water was delivered to the tube wall, that is, the initial flow rate of the dispersed phase was zero. In accordance with the experimental data, calculations were carried out for two initial values of the film flow rate and three different values of the air velocity. We can see that the film flow rate decreases monotonically as a result of separation and entrainment of droplets, with a lower film flow rate corresponding to a higher gas velocity. As it follows from Fig. 2, correlation (24) and (25), especially (24), considerably underestimate the entrainment rate of droplets in the inlet section of the tube, thereby resulting in much higher values of the film flow rate compared with the measurements. On the contrary, correlation (26) predicts too high values of the entrainment rate, thereby appreciably underestimating the film flow rate, except for the region immediately adjacent to the inlet section. The best agreement with the experimental data, excluding the region immediately adjacent to the inlet section, is met when determining the entrainment rate in accordance with (27).

Now let us compare calculations with experimental data as regard to the ratio between the flow rates of the liquid phase in the form of droplets and film. In the literature, this ratio is usually specified by the so-called entrainment coefficient $E \equiv W_2/(W_2 + W_3)$, which is equal to the ratio between the mass flow rate of the dispersed phase (droplets) and the total flow rate of the liquid (droplets and film). In two-fluid models, the entrainment coefficient has to be prescribed by certain correlation; therefore, a number of empirical correla-

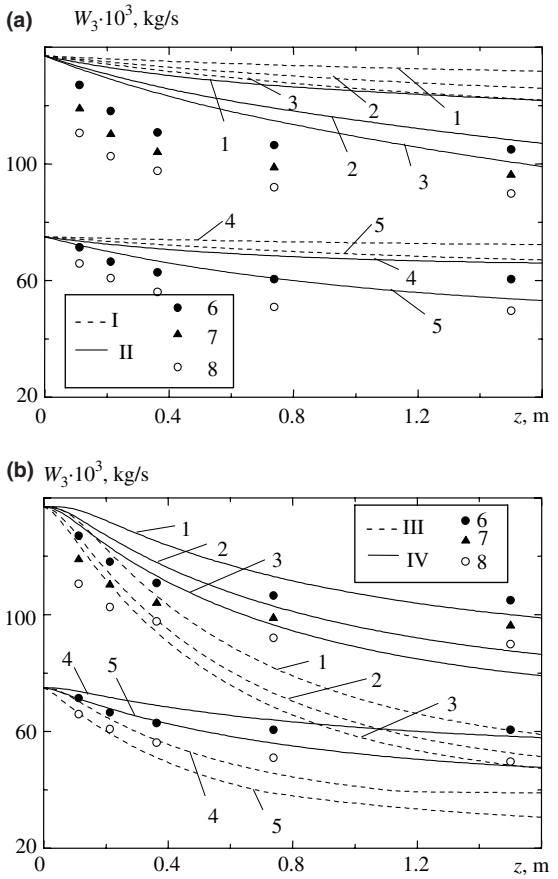

Fig. 2. Variation in the film flow rate over the channel length at $P = 0.3$ MPa. (a) I and II: Calculations using (24) and (25); (b) III and IV: calculations using (26) and (27); 1–3: $W_{30} = 0.137$ kg/s; 4, 5: $W_{30} = 0.075$ kg/s; 6–8: experiment [24]; 1, 4, 6: $U_G = 15.5$ m/s; 2, 7: $U_G = 23.5$ m/s; 3, 5, 8: $U_G = 28$ m/s.

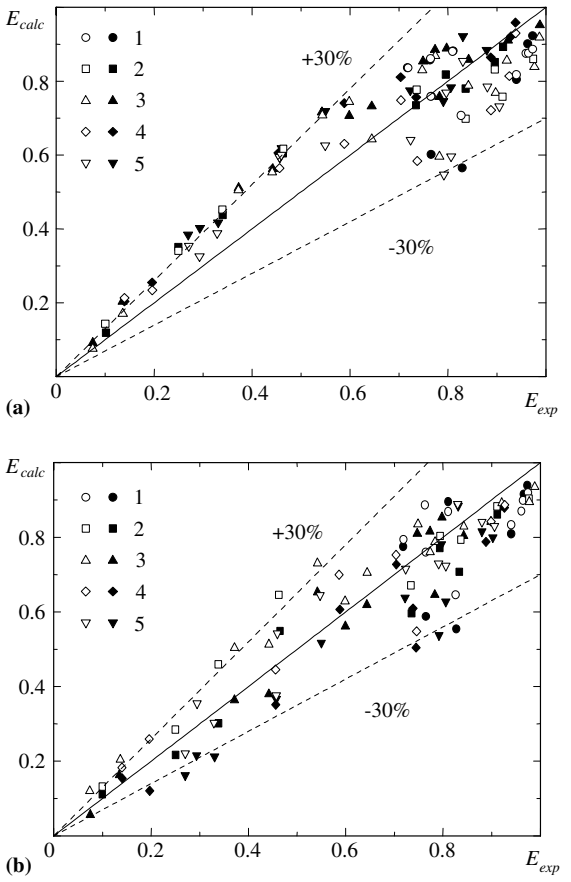

Fig. 3. Comparison of the predicted entrainment coefficients with experimental data [42]. (a) Hollow and solid points: calculations by (24) and (25); (b) hollow and solid points: calculations by (26) and (27); 1–5: $P = 1, 3, 5, 7, 10$ MPa.

tions for determining E have been suggested to date (for example, see Ishii and Mishima [41]). However, such correlations, as a rule, fail to provide an adequate description of the distribution of the liquid outside of the range of the experimental data used to derive these. The three-fluid model enables to simulate the entrainment coefficient without involving additional empirical information other than that used in closing the set of transport balance equations. The entrainment coefficients predicted were compared with the experimental data reported in [42] for hydrodynamically developed flows away from the channel inlet, where dynamic equilibrium between the processes of droplet deposition and entrainment being set. The experiments were carried out in channels of different diameters ($D = 8$–30 mm) and cover a wide range of pressure ($P = 1$–16 MPa) and superficial mass flow rate ($\dot{m} = 500$–4000 kg/m^2 s). The results of comparison of the predicted and measured values of the entrainment coefficient are presented in Fig. 3. It is apparent that none of correlations (24)–(27) for the entrainment rate is ideal in the entire range of the determining parameters. Equations (24) and (25) lead to a considerable error in the case of low mass flow rates and void fractions, and (25) provides acceptable results only at moderate pressures. Correlations (26) and (27) also bring about a marked deviation from the experimental values, especially for low values of E.

Of special interest is the behavior of the mass flow rate of the dispersed phase at low values of the gas velocity. Fig. 4 plots the predicted curves and the experiments of Azzopardi and Zaidi [43] for the superficial droplet mass flow rate, $\dot{m}_2 \equiv W_2/S$, as a function of the superficial gas velocity, $U_G \equiv W_1/\rho_1 S$. We see the nonmonotonous variation in $\dot{m}_2(U_G)$ and the increase in $\dot{m}_2$ with a decrease in U_G at low values of the gas velocity. Such a dependence of $\dot{m}_2$ on U_G cannot be predicted by calculations using correlations (24) and (25), which relate the entrainment rate to the deviation of the film Reynolds number from its critical value and, accordance with this,

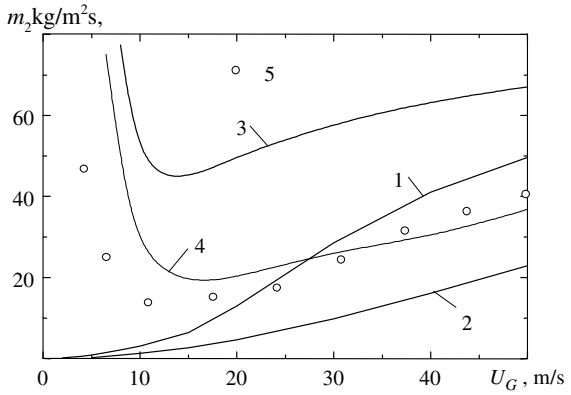

Fig. 4. The superficial droplet mass flow rate as a function of the gas velocity. 1, 2, 3, and 4: Calculations by (24)–(27); 5: experiment [43].

results in reducing $\dot{m}_2$ to zero with decreasing U_G. Earlier this shortcoming of using (24) was point out in [43]. On the other hand, Eqs. (26) and (27), which are based on the correlation between the entrainment rate and the deviation of the film Weber number from its critical value, describe qualitatively correctly the non-monotonous behavior of $\dot{m}_2$ as a function of U_G. Therefore, it seems likely that the correlations based on the deviation of the film Weber number $We_{\delta i}$ from the respective critical value $We^*_{\delta i}$ are more correct than the ones based on the deviation of the film Reynolds number Re_3 from its critical value Re^*_3, and theoretical models for predicting liquid entrainment need to be further refined.

Next let us compare our calculations with the experimental data [44] regarding to the film thickness and the pressure drop. These experiments were accomplished for both downward and upward flow in a vertical tube of the inner diameter of 15 mm. Water and water-glycerine solution were selected as the liquid phase, and air was used as the gas phase. The flow in the measurement section was hydrogynamically stabilized. Calculations performed showed that the values of the film thickness as well as those of the pressure drop obtained by means of any correlation for the entrainment rate of (24)–(27) are rather close to each other. Therefore, Fig. 5 presents only the calculations results obtained by using (27), while Figs. 6 and 7 show those by (25) and (27).

In Fig. 5, the effect of the superficial gas velocity and the water mass flow rate on the film thickness as well as on the pressure gradient is shown. As is seen from Fig. 5(a), the film thickness decreases with increasing the gas velocity, and this is apparently connected with an increase in the mean film velocity. We see also that the film thickness increases monotonically as the liquid flow rate increases. In the upward flow, interfacial stress and gravity act in opposite directions; therefore, the film thickness is found to be somewhat more than that in the downward flow. Fig. 5(b) demonstrates the monotonic growth of the pressure gradient with an increase in both the gas velocity and the water flow rate. Like the film thickness, the pressure gradient in the upward flow has a slightly greater magnitude than that in the downward flow, however, this difference disappears as the gas velocity increases.

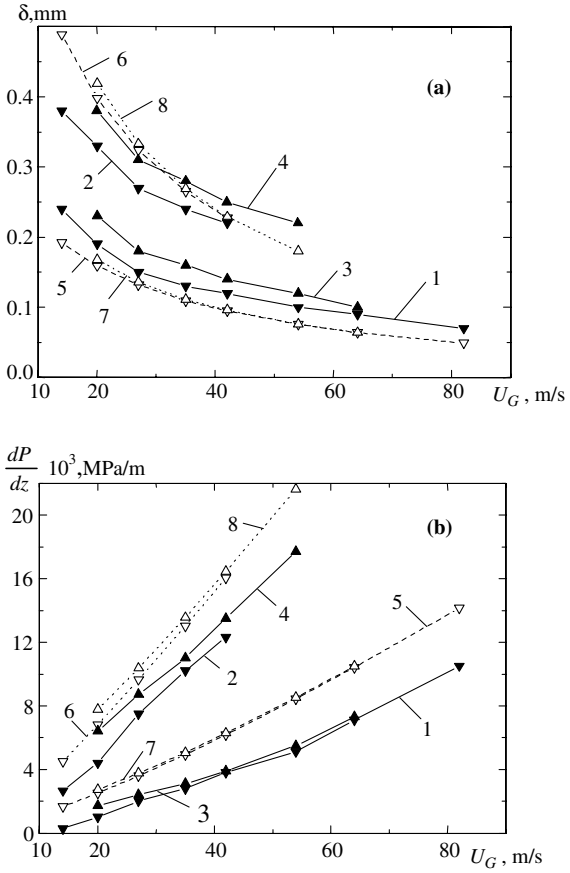

Fig. 5. The film thickness (a) and the pressure gradient (b) as functions of the gas velocity. 1–4: Experiment [44]; 5–8: calculations; 1, 2, 5, 6: downward flow; 3, 4, 7, 8: upward flow; 1, 3, 5, 7: $W_L = 6.7 \times 10^{-3}$ kg/s; 2, 4, 6, 8: $W_L = 49.5 \times 10^{-3}$ kg/s.

Figs. 6 and 7 give comparisons between the predicted and measured values of the film thickness and the pressure drop for all the cases considered in the experiments of Markovich et al. [44]. As is seen, a reasonable agreement exists between the predictions and experiments, although the calculations systematically overestimate the pressure gradient. Moreover, from Figs. 6 and 7, we can conclude that correlations (25) and (27) for the entrainment rate result in very close values of both the film thickness and the pressure drop.

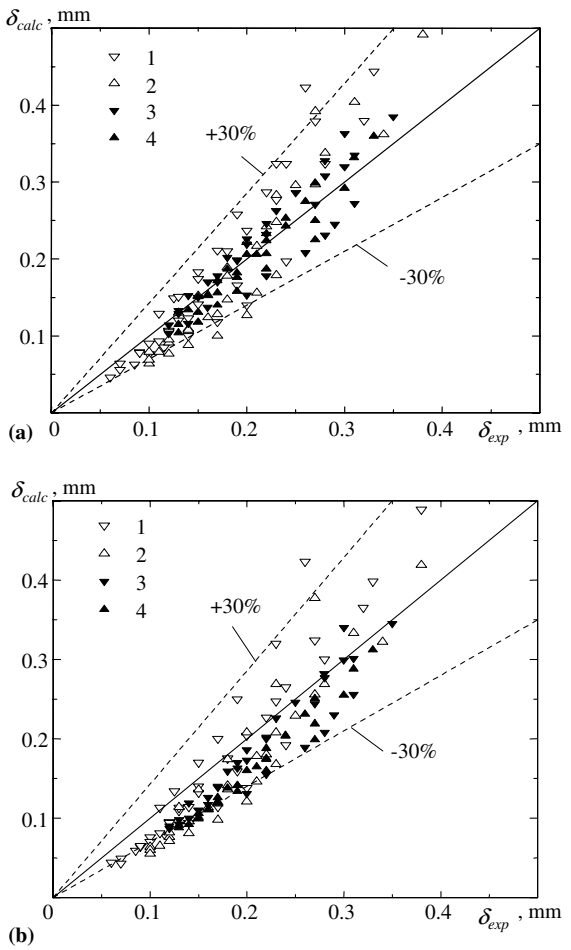

Fig. 6. Comparison of the film thickness predicted and measured by Markovich et al. [44]. (a) Calculation by (25); (b) calculation by (27); 1: downward flow of water; 2: upward flow of water; 3: downward flow of water–glycerine solution; 4: upward flow of water–glycerine solution.

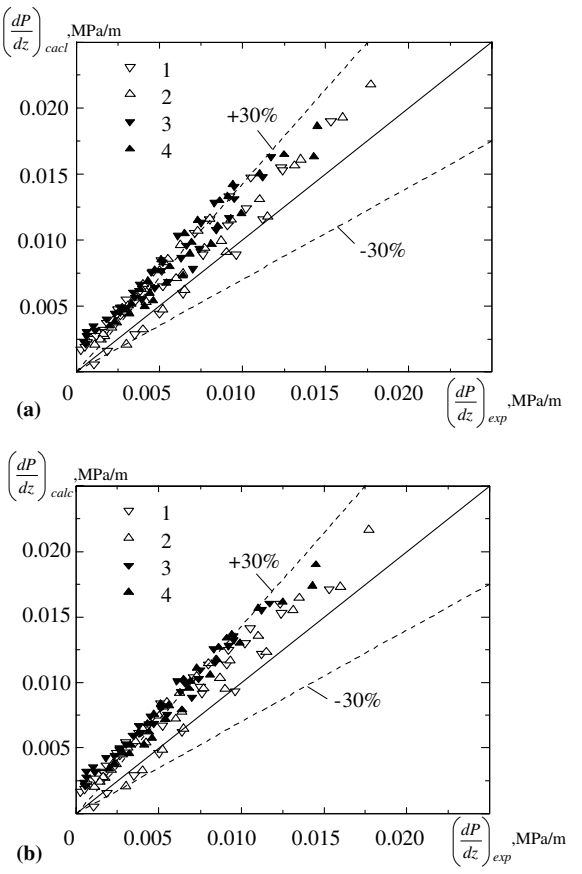

Fig. 7. Comparison of the predicted pressure gradients with experimental data [44], for symbols see Fig. 6.

Finally, let consider comparisons between calculated and measured values of the droplet Sauter diameter. Comparisons have been conducted with the experimental data of Jepson et al. [45], which were performed for air–water and helium–water flows over a fairly wide range of the gas and liquid flow rates. Although the experiments were carried out at one and the same pressure in the system ($P = 1.5$ bar), the comparison of results for air and helium enables to analyze the effect of the gas-to-liquid density ratio ρ_1/ρ_2 and thereby to assess the influence of the major factors quantifying the effect of pressure. Fig. 8 shows typical variations in the Sauter diameter of droplets along the channel. The quantity $\dot{m}_L$ in the caption of Fig. 8 is the superficial mass flow rate of the liquid phase, $\dot{m}_L \equiv (W_2 + W_3)/S$. From Fig. 8, we can see that, in accordance with the experimental data, calculations may predict both a decrease in the droplet size due to breakup and an increase in that due to coagulation. Fig. 8 presents also the predictions corresponding to the familiar correlations of Azzopardi et al. [46] and Azzopardi [47] for the size of droplets in the annular two-phase flow

$$\frac{d_{32}}{D} = 1.91\frac{Re_1^{0.1}}{We_{D1}^{0.6}}\left(\frac{\rho_1}{\rho_2}\right)^{0.6} + 0.4\frac{\alpha_2\rho_2U_2}{\alpha_1\rho_1U_1}, \tag{45}$$

$$\frac{d_{32}}{\lambda} = \frac{15.4}{We_{\lambda 1}^{0.58}}\left(\frac{\rho_1}{\rho_2}\right)^{0.58} + 3.5\frac{\alpha_2\rho_2U_2}{\alpha_1\rho_1U_1}$$

$$\lambda = \left(\frac{\sigma}{\rho_2 g}\right)^{1/2}, \quad We_{\lambda 1} = \frac{\rho_1 U_1^2 \lambda}{\sigma}. \tag{46}$$

The first terms on the right-hand sides of (45) and (46) describe the equilibrium droplet size due to breakup, whereas the second terms take into consideration an increase in the droplet size as a result of coagulation and are proportional to the ratio of the flow rates of the dispersed and gas phases. Note that the second terms in (45) and (46) may be used to allow for the coagulation of droplets only in the case of relatively low values of

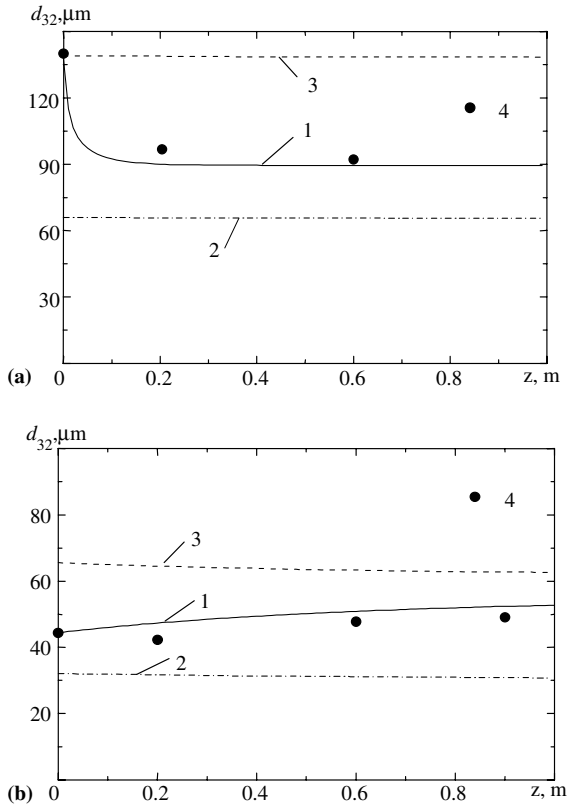

Fig. 8. Variation of the Sauter diameter of droplets in the air flow along the channel. (a) $U_G = 22.22$ m/s, $\dot{m}_L = 120$ kg/m^2 s; (b) $U_G = 44.44$ m/s, $\dot{m}_L = 120$ kg/m^2 s; 1: calculation; 2: correlation [45] of Azzopardi et al. [46]; 3: correlation [46] of Azzopardi [47]; 4: experiment by Jepson et al. [45].

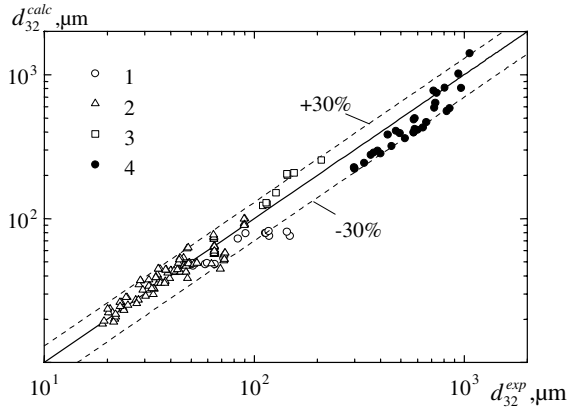

Fig. 9. Comparison of the predicted Sauter diameter of droplets with experimental data. 1: [48]; 2: [45]; 3: [49]; 4: [50].

the flow rate ratio. In the case of high values of $\alpha_2\rho_2U_2/\alpha_1\rho_1U_1$, these terms bring about too large droplet sizes. As follows from Fig. 8, correlation (45) underestimates, and correlation (46) overestimates the measured droplet sizes.

Fig. 9 is a comparison of the predicted Sauter diameters of droplets with the experimental data given in [45,48–50]. We can see that the mean droplet size calculated using the equation for the droplet number density is in a quite good agreement with the experiments under consideration.

8. Summary

A three-fluid model of the two-phase annular flow is presented. This model is based on the conservation equations of mass, momentum, and energy for the gas and dispersed phases, and the film as well as additionally includes the equation for the number density of particles of the dispersed phase. The latter equation is used to determine the mean particle size and may take into account different mechanisms of the particle size variation due to breakup, coagulation, deposition, liquid entrainment from the film, and phase changes. Calculations are performed for the inlet section as well as for the region of hydrodynamically-stabilized flow in channels.

On the basis of thorough comparisons with experimental data, it can be concluded that the three-fluid model developed gives a reasonable description of the processes of deposition, coagulation, and fragmentation and can be successfully applied to predict the entrainment problem in the gas–liquid turbulent annular flows.

As the next step in the development of the three-fluid model, we will employ it to predict critical heat flux and describe heat transfer in the post-dryout region.

References

[1] S. Sugawara, Droplet deposition and entrainment modeling based on the three-fluid model, Nucl. Eng. Des. 122 (1990) 67–84.
[2] R.I. Nigmatulin, Dynamics of Multiphase Media, Hemisphere, New York, 1991.
[3] V. Stevanovic, M.A. Studovic, Simple model for vertical annular and horizontal stratified two-phase flows with liquid entrainment and phase transitions: one-dimensional steady state conditions, Nucl. Eng. Des. 154 (1995) 357–379.
[4] S. Ho Kee King, G. Piar, Effects of entrainment and deposition mechanism on annular dispersed two-phase flow in a converging nozzle, Int. J. Multiphase Flow 25 (1999) 321–347.
[5] G. Kocamustafaogullari, M. Ishii, Foundation of the interfacial area transport equation and its closure relations, Int. J. Heat Mass Transfer 38 (1995) 481–493.
[6] T. Hibilki, M. Ishii, One-group interfacial area transport of bubbly flows in vertical round tubes, Int. J. Heat Mass Transfer 43 (2000) 2711–2726.

[7] H. Schlichting, Boundary Layer Theory, McGraw-Hill, New York, 1968.
[8] G.B. Wallis, One-Dimensional Two-Phase Flow, McGraw-Hill, New York, 1969.
[9] W.H. Henstock, T.J. Hanratty, The interfacial drag and the height of the wall layer in annular flows, AIChE J. 22 (1976) 990–1000.
[10] J.C. Asali, T.J. Hanratty, P. Andreussi, Interfacial drag and film height for vertical annular flow, AIChE J. 31 (1985) 895–902.
[11] W. Ambrosini, P. Andreussi, B.J. Azzopardi, A physically based correlation for drop size in annular flow, Int. J. Multiphase Flow 17 (1991) 497–507.
[12] T. Fukano, T. Furukawa, Prediction of the effects of liquid viscosity on interfacial shear stress and frictional pressure drop in vertical upward gas–liquid annular flow, Int. J. Multiphase Flow 24 (1998) 587–603.
[13] L.B. Fore, S.G. Beus, R.C. Bauer, Interfacial friction in gas–liquid annular flow: analogies to full and transition roughness, Int. J. Multiphase Flow 26 (2000) 1755–1769.
[14] M. Fossa, C. Pisoni, L.A. Tagliafico, Experimental and theoretical results on upward annular flows in thermal non-equilibrium, Exp. Therm. Fluid Sci. 16 (1998) 220–229.
[15] J.O. Hinze, Turbulence, McGraw-Hill, New York, 1975.
[16] L.I. Zaichik, V.M. Alipchenkov, Interaction time of turbulent eddies and colliding particles, Thermophys. Aeromech. 6 (1999) 493–501.
[17] L.I. Zaichik, V.M. Alipchenkov, A statistical model for transport and deposition of high-inertia colliding particles in turbulent flow, Int. J. Heat Fluid Flow 22 (2001) 365–371.
[18] P. Andreussi, Droplet transfer in two-phase annual flow, Int. J. Multiphase Flow 9 (1983) 697–713.
[19] S.A. Schadel, G.W. Leman, J.L. Binder, T.J. Hanratty, Rates of atomization and deposition in vertical annular flow, Int. J. Multiphase Flow 16 (1990) 363–374.
[20] K.J. Hay, Z.-C. Liu, T.J. Hanratty, Relation of deposition to drop size when the rate law is nonlinear, Int. J. Multiphase Flow 22 (1996) 829–848.
[21] G.F. Hewitt, A.H. Govan, Phenomenological modeling of non-equilibrium flows with phase change, Int. J. Heat Mass Transfer 33 (1990) 229–242.
[22] R.I. Nigmatulin, B.I. Nigmatulin, Ya.D. Khodzhaev, V.E. Kroshilin, Entrainment and deposition rates in a dispersed-film flow, Int. J. Multiphase Flow 22 (1996) 19–30.
[23] G.F. Hewitt, N.S. Hall-Taylor, Annular Two-Phase Flow, Pergamon Press, Oxford, 1970.
[24] B.I. Nigmatulin, S.B. Netunaev, M.Z. Gorjunova, Investigation of moisture entrainment processes from the liquid film surface in air–water upflow, Thermophys. High Temp. 20 (1982) 195–197.
[25] L.I. Zaichik, B.I. Nigmatulin, V.M. Alipchenkov, Droplet entrainment in vertical gas–liquid annular flow, in: Proceedings of the 2nd International Symposium on Two-Phase Flow Modelling and Experimentation, Rome, vol. 2, 1999.
[26] M. Ishii, M.A. Grolmes, Inception criteria for droplet entrainment in two-phase concurrent film flow, AIChE J. 21 (1975) 308–318.
[27] M.A. Lopez de Bertodano, A. Assad, Entrainment rate of droplets in the ripple-annular regime for small vertical ducts, Nucl. Sci. Eng. 129 (1998) 72–80.
[28] T.J. Hanratty, L.A. Dykhno, Physical Issues in Analyzing Gas-Liquid Annular Flows, in: Proceedings of the 4th World Conference on Experimental Heat Transfer, Fluid Mechanics and Thermodynamics, Brussels, vol. 2, 1997.
[29] B.J. Azzopardi, Drops in annular two-phase flow, Int. J. Multiphase Flow 23 (Suppl.) (1997) 1–53.
[30] J.O. Hinze, Fundamentals of the hydrodynamics mechanisms of splitting in dispersion process, AIChE J. 1 (1955) 289–295.
[31] I. Kataoka, M. Ishii, K. Mishima, Generation and size distribution of droplets in annular two-phase flow, Trans. ASME J. Fluids Eng. 105 (1983) 230–238.
[32] B.E. Gelfand, Droplet breakup phenomena in flows with velocity lag, Prog. Energy Combust. Sci. 22 (1996) 201–265.
[33] H. Lamb, Hydrodynamics, Cambridge University Press, Cambridge, MA, 1932.
[34] A.S. Monin, A.M. Yaglom, Statistical Fluid Mechanics: Mechanics of Turbulence, vol. 2, MIT Press, Cambridge, 1975.
[35] L.I. Zaichik, V.M. Alipchenkov, Pair dispersion and preferential concentration of particles in isotropic turbulence, Phys. Fluids 15 (2003) 1776–1787.
[36] L.I. Zaichik, V.M. Alipchenkov, A.R. Avetissian, Coalescence and breakup of droplets and bubbles in two-phase turbulent flows, in: Proceedings of the 3rd International Conference on Transport Phenomena in Multiphase Systems, Baranów Sandomierski, Poland, 2002.
[37] M. Sevik, S.H. Park, The splitting of drops and bubbles by turbulent fluid flow, Trans. ASME J. Fluids Eng. 95 (1973) 53–60.
[38] L.I. Zaichik, O. Simonin, V.M. Alipchenkov, Two statistical models for predicting collision rates of inertial particles in homogeneous isotropic turbulence, Phys. Fluids 15 (2003) 2995–3005.
[39] C. Martinez-Bazan, J.L. Montanes, J.C. Lasheras, On the breakup of an air bubble injected into a fully developed turbulent flow. Part 1. Breakup frequency, J. Fluid Mech. 401 (1999) 157–182.
[40] J. Lavieville, E. Deutsch, O. Simonin, Large eddy simulation of interaction between colliding particles and a homogeneous isotropic turbulence field, in: Proceedings of the 6th International Symposium on Gas-Particle Flows, ASME FED, vol. 228, 1995.
[41] M. Ishii, K. Mishima, Droplet entrainment correlation in annular two-phase flow, Int. J. Heat Mass Transfer 32 (1989) 1835–1846.
[42] B.I. Nigmatulin, O.I. Melikhov, I.D. Khodjaev, Investigation of rate of entrainment in a dispersed-annular gas–liquid flow, in: Proceedings of the 2nd International Conference on Multiphase Flow, Kyoto, vol. 3, 1995.
[43] B.J. Azzopardi, S.H. Zaidi, Determination of entrained fraction in vertical annular gas/liquid flow, Trans. ASME J. Fluids Eng. 122 (2000) 146–150.
[44] D.M. Markovich, V.A. Antipin, S.M. Charlamov, A.V. Cherdantchev, Thermophysical and hydrodynamical experiments for verifying the computer code "CORSAR",

Report 01-2405-2001, Institute of Thermophysics, Novosibirsk, Russia, 2001.
[45] D.M. Jepson, B.J. Azzopardi, P.B. Whalley, The effect of gas properties on drops in annular flow, Int. J. Multiphase Flow 15 (1989) 327–339.
[46] B.J. Azzopardi, Drop-sizes in annular two-phase flow, Exp. Fluids 3 (1985) 53–59.
[47] B.J. Azzopardi, G. Freeman, D.J. King, Drop sizes and deposition in annular two-phase flow, UKAEA Report, AERE R9634, 1980.
[48] L.B. Cousins, G.F. Hewitt, Liquid phase mass transfer in annular two-phase flow: droplet deposition and liquid entrainment, UKAEA Report, AERE R5657, 1968.
[49] B.J. Azzopardi, J.C.F. Teixeira, Detailed measurements of vertical annular two-phase flow – Part 1: Drop velocities and sizes, Trans. ASME J. Fluids Eng. 116 (1994) 792–795.
[50] L.B. Fore, B.B. Ibrahim, S.G. Beus, Visual measurements of droplet size in gas–liquid annular flow, in: Proceedings of the 4th International Conference on Multiphase Flow, New Orleans, USA, 2001.